

Modeling and Control of a novel Variable Stiffness three DoF Wrist

Giuseppe Milazzo¹, Manuel Giuseppe Catalano¹, Antonio Bicchi^{1,2}, Giorgio Grioli^{1,2}

Abstract

This paper presents a novel design for a Variable Stiffness 3 DoF actuated wrist to improve task adaptability and safety during interactions with people and objects. The proposed design employs a hybrid serial-parallel configuration to achieve a 3 DoF wrist joint which can actively and continuously vary its overall stiffness thanks to the redundant elastic actuation system, using only four motors. Its stiffness control principle is similar to human muscular impedance regulation, with the shape of the stiffness ellipsoid mostly depending on posture, while the elastic cocontraction modulates its overall size. The employed mechanical configuration achieves a compact and lightweight device that, thanks to its anthropomorphous characteristics, could be suitable for prostheses and humanoid robots.

After introducing the design concept of the device, this work provides methods to estimate the posture of the wrist by using joint angle measurements and to modulate its stiffness. Thereafter, this paper describes the first physical implementation of the presented design, detailing the mechanical prototype and electronic hardware, the control architecture, and the associated firmware. The reported experimental results show the potential of the proposed device while highlighting some limitations. To conclude, we show the motion and stiffness behavior of the device with some qualitative experiments.

Keywords

Variable Stiffness, Articulated Soft Robots, Wrist, Prosthesis.

1 Introduction

One of the challenges of modern robotics is to craft machines that can physically interact and cooperate with people. Taking inspiration from humans, compliant end-effectors have proven their capability to adapt using simple actuation and control systems in various applications, ranging from industrial [Firth et al. \(2022\)](#), [Zongxing et al. \(2020\)](#), to prosthetics [Tavakoli and de Almeida \(2014\)](#) and service robotics [Tröbinger et al. \(2021\)](#). However, to promote the simplicity of the hardware, robotic limbs usually equip rigid and underactuated serial wrist joints [Bajaj et al. \(2019\)](#). Nonetheless, wrist articulation plays a crucial role in manipulation tasks since it allows for varying the hand pose to reach the best posture for grasping an object. Therefore, a complete wrist joint should feature 3 DoFs to orient the end-effector in a tridimensional space freely.

Many studies prove that human beings adjust the stiffness of their limbs by exploiting muscular cocontraction to adapt to tasks of different natures. In summary, a large stiffness performs better in resisting perturbations and accomplishing precision tasks, while a soft behavior is more suitable for other assignments, e.g., those that require exploring an unknown environment with small interaction forces [Blank et al. \(2014\)](#), [Borzelli et al. \(2018\)](#), [Osu et al. \(2004\)](#). Therefore, it is desirable to replicate this feature of controllable impedance also in robots. One possible way is to adjust the stiffness of rigid manipulators via software, taking advantage of established impedance control techniques [Hogan \(1985\)](#), [Yellewa et al. \(2022\)](#).

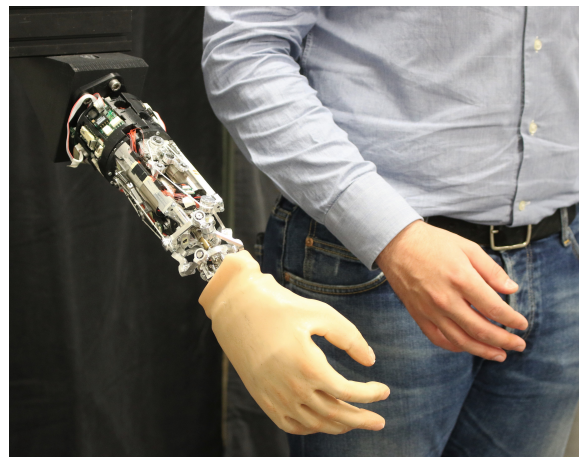


Figure 1. The VS-Wrist compared to a human forearm.

Another possibility is employing soft robots that embed the Variable Stiffness (VS) ability in the hardware implementation. In contrast to classical machines, soft robots

¹Soft Robotics for Human Cooperation and Rehabilitation, Istituto Italiano di Tecnologia, Genova, Italy

²Centro di Ricerca Enrico Piaggio, Università di Pisa, Pisa, Italy.

Corresponding author:

Giuseppe Milazzo, Soft Robotics for Human Cooperation and Rehabilitation, Istituto Italiano di Tecnologia, Via S. Quirico, 19d, 16163, Genova, Italy.

Email: giuseppe.milazzo@iit.it

are more suitable for applications where the device interacts with the environment since safety and robustness become the main requests, replacing power and precision requirements typical of industrial manipulators. Articulated soft robots achieve this goal by embedding compliant elements in their actuation or transmission, resulting in a behavior comparable to that of the musculoskeletal system of animals [Migliore et al. \(2005\)](#). In addition, using redundant non-backdrivable actuators, the elastic elements can apply constant forces to increase the stiffness of the joint without requiring a continuous input of energy.

Passive stiffness regulation has several advantages when compared to impedance control. Active systems use measurements of joint movement and interaction forces to modulate feedback gains, thus changing the effective stiffness of the joint. However, actively controlling the impedance in torque-controlled robots and in backdrivable variable stiffness joints requires either high computational cost or a constant energy drain. Those drawbacks are particularly relevant to mobile robots and prostheses, where the entire device must match restrictive size and weight constraints that limit the computational power and battery capacity [English and Russell \(1999\)](#). Moreover, [Haddadin et al. \(2007\)](#) shows that, concerning safety, even if the impacts are detected timely, the motors could not react fast enough by solely an impedance control, so the system should be considered stiff during the impacts, therefore making impedance controlled robots potentially dangerous. On the contrary, compliant mechanisms protect the device in case of external impacts by decoupling the output link from the rest of the system. Furthermore, soft robots are more robust since they can remain compliant even when the actuators are disabled or faulty [Albu-Schaffer et al. \(2008\)](#). In addition, the energy stored in the elastic elements could reduce the power consumption of the system and enhance the motor abilities in explosive movements and cyclic tasks [Albu-Schaffer et al. \(2008\)](#), [Haddadin et al. \(2011\)](#), [Grioli et al. \(2015\)](#).

Despite the numerous advantages of Variable Stiffness (VS) actuation, commonly, artificial wrists do not implement this feature. Some commercial passive wrists¹ embed elastic elements to comply with the flexion/extension movements [Archer et al. \(2011\)](#). Yang et al. present a serial 2 DoF soft wrist made of the sequence of two continuum bending and torsion modules, which can continuously vary the stiffness of the bending joint by inflating a balloon [Yang et al. \(2022\)](#). Von Drigalski et al. show a passive 6 DoF wrist for industrial applications with inherent compliance, which can switch to the rigid configuration using an external actuator [von Drigalski et al. \(2020\)](#). Recently, other researchers employed powered one DoF VS joints for elbow [Lemerle et al. \(2019\)](#), [Baggetta et al. \(2022\)](#) and ankle prostheses [Agboola-Dobson et al. \(2019\)](#), and motor rehabilitation devices [Liu et al. \(2018\)](#); [Chen et al. \(2021\)](#), thanks to their affinity with the human musculoskeletal system. However, there still is a lack of fully actuated 3 DoF wrist joints with variable stiffness.

This work presents a novel and compact Variable Stiffness wrist with 3 DoFs, shown in Figure 1, which can actively vary its overall stiffness with continuity, and, thanks to its anthropomorphous characteristics, could be suitable for prostheses and humanoid robots. This paper extends the mathematical model of a concept already

introduced in [Lemerle et al. \(2021\)](#) and [Lemerle \(2021\)](#), and validates the effectiveness of the idea with the first hardware implementation. Section 2 explains the general design concept of the device, and Section 3 describes its model. A detailed report of the hardware implementation follows in Section 5, focusing on the elastic transmission mechanism in Section 4. Subsequently, Section 6 depicts the employed control strategy. Section 8 reports the experimental evaluation of the performance using a Motion Capture system and shows some practical applications of the device. Finally, Section 10 discusses the system applications, highlighting our future developments.

2 Design Concept

The VS-Wrist features a hybrid serial-parallel architecture that takes advantage of the redundancy of the actuation system and a non-linear elastic transmission to adjust the stiffness of the coupler. It comprises a 2 DoF VS joint achieved with a Parallel Manipulator (PM) architecture, and an additional serial motor unit, decoupled from the variable stiffness mechanism.

Figure 2a shows the general architecture of the 2 DoF VS joint. Note that, as discussed in [Lemerle et al. \(2021\)](#), its leg kinematics is inspired by that of the Omni-Wrist III in [Rosheim and Sauter \(2002\)](#). However, the proposed design features only three legs instead of four and presents some substantial differences in the actuation system to enable the modulation of the joint stiffness. Precisely, the 2 DoF VS joint includes in its design a supplementary actuator and a non-linear elastic mechanism to transmit the motion of each motor to the first joint of each kinematic chain.

Figure 2b shows the mechanical design of the VS-Wrist and describes its degrees of freedom. In this regard, the PM achieves the ulnar/radial deviation and the flexion/extension of the wrist, while the serial motor unit actuates the wrist along the pronation/supination (PS) axis. Unlike the human wrist, this last motor unit only rotates the hand instead of the whole forearm.

The VS-Wrist presents an innovative mechanical structure that embodies part of the system intelligence. Usually, an n degree of freedom VS joint would require $2n$ motors to control its position and stiffness. Using a PM, it is possible to adjust the stiffness of the wrist by exploiting internal torques, employing only three motors to control two DoFs in position and leaving one DoF to regulate the overall stiffness of the coupler. Therefore, the PM architecture achieves a two DoF variable stiffness joint with the minimum possible number of motors, thus obtaining a compact and lightweight device. This design choice agrees with the human mechanism of muscular impedance regulation since muscular cocontraction mostly modulates the compliance ellipsoid dimensions, while the orientation of its axes essentially depends on the posture [Ajoudani et al. \(2018\)](#).

3 System Analysis

To study the device behavior, we start the kinematic analysis considering the PM alone. Then, we add the effect of the serial motor unit since its rotation does not affect the PM kinematics. Define the reference coordinate

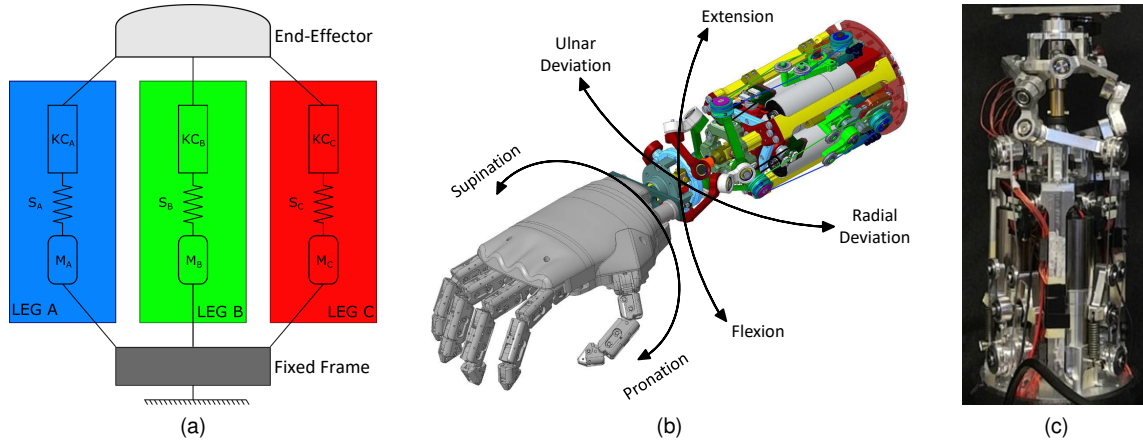


Figure 2. Panel (a) depicts a schematic architecture of the 2 DoF VS joint that is part of the VS-Wrist. Its kinematic configuration is a parallel manipulator that achieves hemispherical movements of the coupler. Each leg is highlighted in one specific color and comprises a motor unit, a non-linear elastic transmission, and a kinematic chain of four revolute joints. Panel (b) displays the CAD of the VS-Wrist equipping the Pisa/IIT SoftHand and highlights its DoFs. Panel (c) shows a close-up picture of the prototype.

frames $\{S_b\}$, fixed to the base of the wrist, and $\{S_e\}$, attached to the coupler. The pose of the end-effector with respect to the fixed frame $\{S_b\}$ can be parametrized by the vector $\mathbf{x} = (\alpha_x \ \alpha_y \ \alpha_z \ x_e \ y_e \ z_e)^T$, whose first three components are Euler angles and the last three defines the position of the origin of frame $\{S_e\}$, fixed to the center of the coupler. However, since the PM has 2 DoFs, the minimum parametrization $\mathbf{u} = (\alpha_y \ \alpha_z)^T$, i.e., the ulnar/radial deviation and the flexion/extension angles of the wrist, univocally determines its pose.

Define the homogeneous transformation matrices $T_{T^*}(p)$ and $T_{R^*}(p)$ that respectively encode a translation and a rotation, along the generic $*$ axis, of the quantity p . Coherently with the analysis provided in Lemerle et al. (2021), the matrix $T_b^e(\mathbf{x})$, which encodes the pose \mathbf{x} of $\{S_e\}$ w.r.t. $\{S_b\}$, is

$$T_b^e(\mathbf{x}) = \begin{array}{c} T_{T_z}(z_e)T_{T_y}(y_e)T_{T_x}(x_e) \\ T_{R_z}(\alpha_z)T_{R_y}(\alpha_y)T_{R_x}(\alpha_x) \end{array} = \begin{pmatrix} c_z c_y & c_z s_x s_y - s_z c_x & c_z s_y c_x + s_z s_x & x_e \\ s_z c_y & s_z s_x s_y + c_z c_x & s_z s_y c_x + c_z s_x & y_e \\ -s_y & s_x c_y & c_x c_y & z_e \\ 0 & 0 & 0 & 1 \end{pmatrix}, \quad (1)$$

where c_k and s_k stand respectively for $\cos(\alpha_k)$ and $\sin(\alpha_k)$. The transformation matrix T_b^e can also be obtained from the joint angles of a single leg $\mathbf{q} = (q_1 \ q_2 \ q_3 \ q_4)^T$. Parametrize every kinematic chain of the manipulator according to the Denavit-Hartenberg convention, as shown for a generic leg in Figure 3 and Table 1, and assemble the intermediate transformations in local frames to obtain

$$T_b^e(\mathbf{q}) = T_b^0(\eta)T_0^1(q_1)T_1^2(q_2)T_2^3(q_3)T_3^e(q_4), \quad (2)$$

where $T_{i-1}^i = T_{R_z}(q_i)T_{T_z}(d_i)T_{R_x}(\alpha_i)T_{T_x}(a_i)$ defines the homogeneous transformation matrix between subsequent local frames. The PS rotation axis is always parallel to the x-axis of the reference coordinate frame $\{S_e\}$. Therefore, indicating with θ_{PS} the related motor angle, the resulting homogeneous transformation matrix becomes

$$T_b^{e'}(q, \theta_{PS}) = T_b^e(q)T_{R_x}(\theta_{PS}). \quad (3)$$

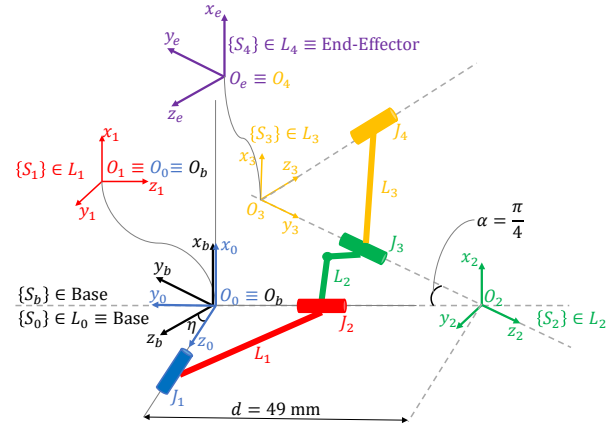


Figure 3. Definition of the local reference coordinate frames of a generic leg according to the Denavit-Hartenberg convention. d , η , and α are fixed design parameters. Aligning the fixed base frame $\{S_b\}$ with the first local frame of leg A $\{S_{A_0}\}$, it follows $\eta_A = 0$, $\eta_B = \frac{2}{3}\pi$, and $\eta_C = \frac{4}{3}\pi$.

Table 1. Denavit-Hartenberg parametrization of a generic leg of the PM. $d = 49$ mm, $\alpha = \frac{\pi}{4}$ are fixed design parameters.

$\{S_{i-1}\} \rightarrow \{S_i\}$	q_i	d_i	a_i	α_i
$\{S_b\} \rightarrow \{S_0\}$	0	0	0	η
$\{S_0\} \rightarrow \{S_1\}$	q_1	0	0	$\pi/2$
$\{S_1\} \rightarrow \{S_2\}$	q_2	d	0	$-\alpha$
$\{S_2\} \rightarrow \{S_3\}$	q_3	$-d$	0	$\pi/2$
$\{S_3\} \rightarrow \{S_e\}$	q_4	0	0	$\pi - \eta$

3.1 Pronation/Supination Transmission Kinematics

The kinematic chain that conveys the motion from the PS motor to the end-effector comprises two Universal Joints (UJs) whose rotation centers coincide with the origins of the reference frames $\{S_b\}$ and $\{S_e\}$. Figure 4 shows the schematization of the PS transmission kinematic

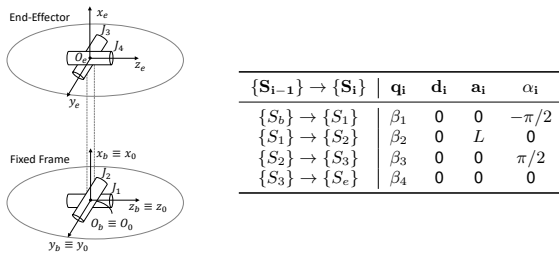


Figure 4. Schematic representation of the double UJ transmission. Each UJ is represented with two perpendicular and incident revolute joints, located either at the center of the fixed base frame or the center of the coupler. Note that the upper and lower UJs are 90° out of phase to cancel the changing angular velocity of the driving shaft introduced by the lower UJ. The table on the right resumes the Denavit-Hartenberg parametrization of the kinematic chain. $L = d\sqrt{2(1 - \cos(\alpha))} = 37.5$ mm is a fixed design parameter.

chain and resumes the definition of the local reference frames according to the Denavith Hartenberg convention. Therefore, the UJ angles $\beta = [\beta_1 \ \beta_2 \ \beta_3 \ \beta_4]^T$ parametrize the homogenous transformation matrix from $\{S_b\}$ to $\{S_e\}$ as

$$T_b^e(\beta) = T_b^1(\beta_1)T_1^2(\beta_2)T_2^3(\beta_3)T_3^e(\beta_4), \quad (4)$$

To simplify the resolution of the inverse kinematics, it is possible to divide the problem into two pieces. The position of the origin $O_2 \equiv O_e$ does not depend on the angles of the second UJ. Therefore, equating

$$O_2(\beta_1, \beta_2) = T_b^2(1 : 3, 4) = T_b^e(1 : 3, 4) = O_e \quad (5)$$

yields

$$\begin{cases} \beta_1 = \text{atan2}(y_e, x_e) \\ \beta_2 = \text{atan2}\left(-z_e, \frac{y_e}{\sin(\beta_1)}\right) \end{cases}. \quad (6)$$

For the second UJ, compute $T_2^e = T_b^{2-1}T_b^e$ to obtain

$$\begin{cases} \beta_3 = \text{atan2}(T_2^e(1, 3), -T_2^e(2, 3)) \\ \beta_4 = \text{atan2}(T_2^e(3, 1), T_2^e(3, 2)) \end{cases}. \quad (7)$$

Moreover, the PM kinematics force the tilt angles of the UJs to be pairwise equal, obtaining $\beta_3 = \beta_2$, and $\beta_4 = \beta_1$.

3.2 Single Leg Forward Kinematics

The transformation matrix $T_b^e(q)$ that encodes the pose of the end-effector w.r.t. the fixed base coordinate frame using the joint angles q , must be the same as $T_b^e(\mathbf{x})$, obtained employing the Euler angles parametrization \mathbf{x} .

Equating these two matrices and solving for \mathbf{x} yields

$$\begin{cases} x_e = T_{1,4}(q) \\ y_e = T_{2,4}(q) \\ z_e = T_{3,4}(q) \\ \alpha_x = \text{atan2}(T_{3,2}(q), T_{3,3}(q)) \\ \alpha_y = \text{atan2}\left(-T_{3,1}(q), \sqrt{T_{3,2}(q)^2 + T_{3,3}(q)^2}\right) \\ \alpha_z = \text{atan2}(T_{2,1}(q), T_{1,1}(q)) \end{cases}, \quad (8)$$

where $T_{i,j}(q)$ is the element of the $T_b^e(q)$ matrix, located at the i th row and j th column. Therefore, provided all the joint angles of a single leg, (8) gives the pose of the end-effector with respect to the fixed frame $\{S_b\}$.

3.3 Inverse Kinematic Problem

Given the pose of the end-effector \mathbf{x} , the answer to the Inverse Kinematic (IK) problem provides the joint angles of the considered leg. Taking advantage of the geometrical constraints

$$\begin{cases} q_3 = q_2 + \pi \\ q_4 = -q_1 \end{cases}, \quad (9)$$

that hold for the mounting arrangement chosen for the legs Sofka et al. (2006), and following the procedure reported in Lemerle et al. (2021), the solution to the IK problem is

$$\begin{cases} q_1 = \text{atan2}\left(\frac{x_e(1 - c_\alpha) + (y_e c_\eta + z_e s_\eta)s_\alpha s_2}{d(1 - c_\alpha)(2 - (1 + c_\alpha)c_2^2)}\right) \\ q_2 = -\text{acos}\left(\frac{y_e \sin(\eta) - z_e \cos(\eta)}{d \sin(\alpha)}\right) \\ q_3 = q_2 + \pi \\ q_4 = -q_1 \end{cases}, \quad (10)$$

where s_2 and c_2 stand for $\sin(q_2)$ and $\cos(q_2)$.

3.4 Parallel Mechanism Forward Kinematics

By equating the transformation matrices obtained using the joint angles of different legs, it is possible to derive all the joint variables of a single kinematic chain as a function of the sole sensorized joint angles, which are the first ones of each leg. Computing x_e and y_e as functions of the joint angles of alternatively legs A and B yields

$$\begin{cases} T_{1,4}(q_A) = x_e(q_A) = x_e(q_B) = T_{1,4}(q_B) \\ T_{2,4}(q_A) = y_e(q_A) = y_e(q_B) = T_{2,4}(q_B) \end{cases}. \quad (11)$$

Taking advantage of (9) and aligning the fixed base frame with the first local frame of leg A (hence $\eta_A = 0$), it is possible to solve the first equation of (11) to obtain

$$s_{A_2} = \frac{(s_{B_1} - s_{A_1})(1 - c_\alpha) + s_\alpha c_{B_1} s_{B_2}}{s_\alpha c_{A_1}}, \quad (12)$$

where s_{*n}, c_{*n} indicate the sine and cosine of the n -th joint angle of the leg $*$. Substitute the previous result in the second equation of (11) to get

$$q_{B_2} = \text{atan2}\left(\frac{\sqrt{2}(s_\alpha t_5 - t_1 \sqrt{h_1 + h_2})}{t_1(1 - t_3 - t_2 c_{\eta_B} + c_{A_1} s_{\eta_B} s_\alpha)}\right), \quad (13)$$

where $t_1, t_2, t_3, t_4, t_5, h_1, h_2 \in \mathbb{R}$ are defined as

$$\begin{cases} t_1 = c_\alpha - 1 \\ t_2 = c_{A_1} c_{B_1} \\ t_3 = 1 + c_{\eta_B} \\ t_4 = c_{A_1}^2 + c_{B_1}^2 \\ t_5 = c_{\eta_B} c_{A_1} s_{B_1} - c_{B_1} s_{A_1} \\ h_1 = t_4 - t_2^2(1 + c_{\eta_B}^2) \\ h_2 = t_1(1 - t_2) - 2t_2 t_3 c_{\eta_B} \end{cases}. \quad (14)$$

Since the measurements of the magnetic encoders provide q_{A_1} and q_{B_1} , (13) and (9) produce all the joint angles of leg B, and (8) provides the pose of the end-effector \mathbf{x} as a function of the sole sensorized variables.

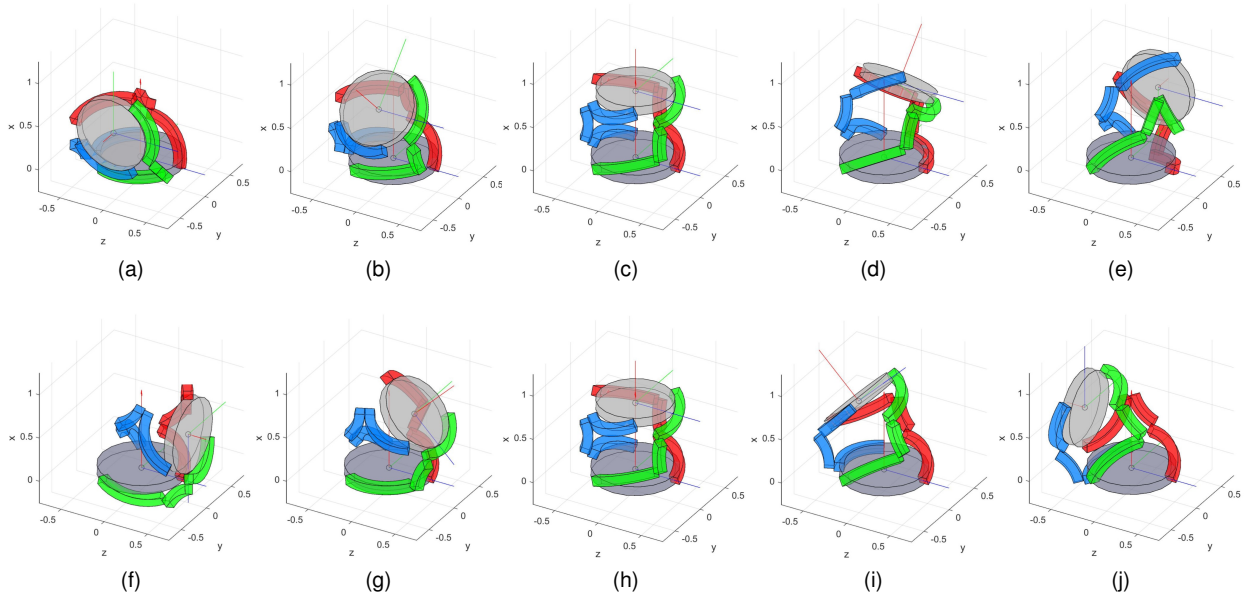


Figure 5. Photo sequence of the kinematic behavior of the system based on the inverse kinematic model. Panels (a) to (e) stand for a motion around the y_b axis, while panels (f) to (j) represent a revolution around the z_b axis (from 90° to -90°).

3.5 Static Equilibrium

The approach consists of solving a classic geometrical problem, opening the kinematic chains in correspondence to their last joint to impose the equilibrium of the end-effector subject to the resulting external wrench and the reaction forces of the coupling joints. Finally, the constraints of these joints are restored by imposing the equilibrium of each leg subject to the previously computed reaction forces. This procedure, reported in detail in Appendix A, yields

$$\begin{cases} \tau_A = J_A^T(q)H^T(q)\tilde{w} & (15a) \\ \tau_{\bar{A}} = J_{\bar{A}}^T(q)H^T(q)\tilde{w} = 0_{9 \times 1} & (15b) \\ w_E = -G(q)H^T(q)\tilde{w} & (15c) \end{cases}$$

where (15a) expresses the equilibrium of the actuated joints, (15b) defines the balance of the torques on the non-actuated joints (that must be null), and (15c) imposes the equilibrium of the end-effector. Since GH^T is a fat matrix with full row rank, all the possible solutions are expressed by

$$\tilde{w} = -(GH^T)^R w_{ext} + P\Lambda, \quad (16)$$

where $(GH^T)^R$ is a right-inverse of GH^T , the columns of P form a basis of the $\mathcal{N}ull(GH^T)$, and Λ is a vector of coefficients that parametrizes the constraint wrenches that achieve the static equilibrium of the end-effector.

The solution of (15a) is:

$$\tau_A = -J_A^T H^T (GH^T)^R w_{ext} + J_A^T H^T P \Lambda, \quad (17)$$

where Λ must satisfy (15b), leaving only one DoF $\lambda \in \mathbb{R}$ that acts on the internal forces of the 2 DoF VS joint through the basis N_0 , defined in Lemerle et al. (2021). Thanks to the non-linear elastic transmission, the actuated torque acting on each leg is a non-linear function of the deflection $\delta = q_1 - \theta_m$ between the first joint and motor angles, thus $\tau_{act} =$

$f(\delta)$. Therefore, the stiffness of the elastic transmission $K(\delta) = -\frac{\partial \tau_{act}}{\partial \delta}$ varies with the deflection. Modulating the internal forces through the parameter λ also affects the active deflection of the elastic elements, thus the stiffness of the manipulator through the non-linearity of the elastic transmissions.

4 Elastic Transmission Mechanism

The output torque of the non-linear elastic mechanism is a function of the design parameters and the deflection between the first joint and motor angles. We derive an analytical function of the output torque using the lever angle γ , defined in Figure 6, to compute the elastic energy as

$$U_s(\gamma) = \frac{1}{2}k(L(\gamma) - L_0)^2, \quad (18)$$

where

$$L(\gamma) = \sqrt{(l_n \sin(\gamma) + d_0)^2 + (l_n(1 - \cos(\gamma)))^2}, \quad (19)$$

is the length of the spring as a function of γ , L_0 is the spring free length, d_0 is its length computed for $\gamma = 0$, and l_n is the length of the horizontal lever arm. Differentiate (18) to obtain

$$\tau(\gamma) = -\frac{\partial U_s}{\partial \delta} = -\frac{\partial U_s}{\partial \gamma} \frac{\partial \gamma}{\partial \delta} = -\frac{\partial U_s}{\partial \gamma} \left(\frac{\partial \delta}{\partial \gamma}\right)^{-1}. \quad (20)$$

by composing the partial derivatives with respect to γ . The relationship $\delta(\gamma, L_t)$ can be found by imposing the conservation of the tendon length L_t , as described in Appendix B. Therefore, given δ from the measurements of the encoders and assuming L_t known by design, it is possible to compute γ , thus the actuated torque.

To obtain the stiffness of the elastic transmission K , it is sufficient to differentiate the output torque w.r.t. the

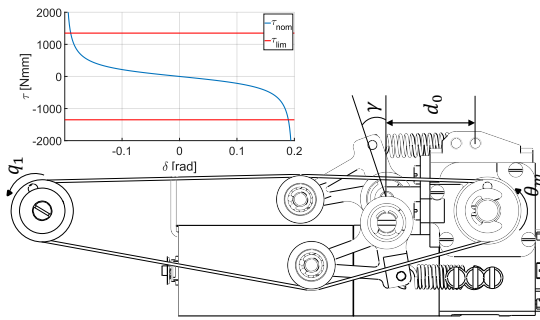


Figure 6. Scheme of the non-linear elastic transmission mechanism and definition of its geometry. The plot in the top-left corner depicts the nominal output torque as a function of the deflection δ .

deflection δ as

$$K(\gamma) = -\frac{\partial \tau_{joint}}{\partial \delta} = -\frac{\partial \tau_{joint}}{\partial \gamma} \left(\frac{\partial \delta}{\partial \gamma}\right)^{-1}. \quad (21)$$

5 Hardware Description

5.1 Mechanical Hardware

Figure 7 shows the CAD of the VS-Wrist and its overall dimensions. The diameter of the fixed frame (in dark red) is 70 mm, whereas the diameter of the end-effector (in yellow) is 60 mm, and the total length of the system is 170 mm. The overall weight of the device is 1110 grams, excluding the hand. These dimensions and weight fit the average sizes of a human wrist and forearm, extracted from NASA (1995). To maintain high stiffness levels without consuming any power, we decided to employ a non-backdrivable actuation system for the 2 DoF VS joint.

The VS joint features three identical sides composed of the serial arrangement of a motor unit (in blue), a non-linear elastic transmission (in green), and a kinematic chain of four non-coplanar revolute joints (in magenta). The motor unit comprises a DCX19S GB KL 12V motor from Maxon, its associated gearbox, and a low-efficiency worm gear transmission to ensure the non-backdrivability of the system. Thanks to this design choice, the springs can apply constant forces that increase the stiffness of the joint without requiring a continuous input of energy. The resulting transmission ratio is 420, with an efficiency of 0.2824. The maximum continuous torque deliverable to the gearbox output shaft is $\tau_{lim} = 1351$ N mm.

The kinematic chains distribute evenly around the fixed frame of the wrist and are made of aluminum alloy to obtain a good trade-off between a lightweight design and resistance to internal tensions and bending. The characteristic length $d = 49$ mm and angular deviation $\alpha = \frac{\pi}{4}$ are such to avoid any internal collision between different legs.

The non-linear elastic system, shown in Figure 6, uses an antagonistic setup of linear springs, tendons, and pulleys to achieve non-linearity thanks to the geometry of the arrangement. One end of the elastic elements is fixed to the frame, while the other attaches to the lever arm mechanism that regulates the tension of the tendons. The employed elastic elements are the extension springs T31320 from

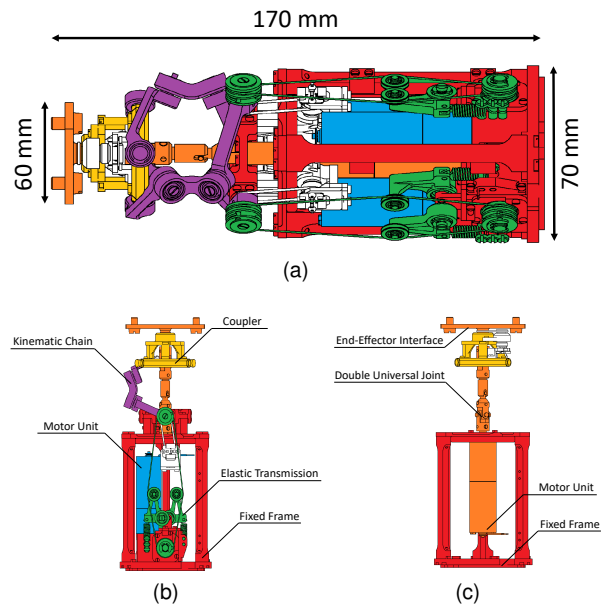


Figure 7. CAD of the VS-Wrist. Every color highlights a different macro-component: red for the fixed frame, light blue for the 2 DoF VS joint motor units, green for the elastic transmission mechanism, magenta for the kinematic chains, orange for the PS unit, and yellow for the end-effector. Panel (a) displays an overall 3D view of the device. Panel (b) shows in detail the implementation of one leg with its variable stiffness unit, and panel (c) portrays the PS unit.

MeterSprings, and the rope used to craft the tendons is Liros DC120 from Unlimited Rope Solutions. A high-precision machine pulled the cables at 90 % of their maximum tolerated tension to prevent their measure from varying during the usual operation of the VS-Wrist.

Figure 7c shows the mechanical implementation of the PS unit. The double UJ structure compensates for parallel misalignment and non-constant velocities between the driving and driven shafts. The transmission is independent of the VS unit, so the stiffness of the joint is not modified by this motor.

5.2 Electronic Hardware

The device employs the NMMI electronics described in Della Santina et al. (2017b). Four independent PID controllers regulate the position of the DC motors using the feedback of four rotary magnetic encoders, which measure the angle θ of the gearbox output shafts. Three additional encoders measure the first joint angle q_1 of each kinematic chain. The 12-bit programmable encoders AS5045 from Austriamicrosystems² provides an instant indication of the output shaft angular position with a resolution of 0.0879°. Four motor drivers, MC33887 from NXP Semiconductors, independently drive the DC motors. The output load is pulse-width modulated at 1 kHz to regulate the current flowing to the motor. The Programmable System-on-Chip (PSoC) 5LP CY8C58LP from Cypress manages the PID controller at a frequency of 1Khz. The embedded microcontroller is a 32-bit Arm Cortex-M3 core plus DMA. A daisy-chain connection allows the different boards to communicate and deliver power from a single DJI TB47 (4500mAh) battery.

Similarly, we can connect other compatible devices, such as the Pisa/IIT SoftHand and the VS-Elbow, and control them with a single interface. The PSoC connects to the computer via micro-USB, and the serial protocol RS485 handles the communication.

6 Control Architecture

For simplicity, we implement an open-loop control law to validate the efficacy of the proposed hardware without altering the inherent system compliance [Della Santina et al. \(2017a\)](#). The control strategy exclusively exploits kinematic considerations to regulate the position of the motors and thus is independent of the characteristic of the non-linear elastic transmission. The control law comprises a position controller and a stiffness controller, which are decoupled and work in parallel.

6.1 Stiffness Control

As described in Section 3.5, the internal forces deliverable through the actuation system $\tau_{stiff} = \lambda N_0$ achieve the stiffness regulation. Although the base of the actuated torques depends exclusively on the kinematics of the manipulator, deriving the motor angles that obtain these torques requires perfect knowledge of the elastic transmission mechanism model. However, manufacturing variability and non-modeled phenomena, such as hysteresis and tendon stretching, limit the accuracy of the derived model.

Therefore, for simplicity, the various stiffness configurations are obtained by commanding the same motor angle δ_{ref} to each VS unit. By doing so, the springs of one branch of all the VS units simultaneously extend while the wrist remains in the central position due to the parallel kinematic constraints. Since the motor angles change while the joints are not moving, this strategy modulates the stiffness of the coupler acting on the deflection of the VS units.

6.2 Position Control

The posture controller exploits the knowledge that the system will tend to reach the static equilibrium where the elastic energy stored in the springs is minimum. Under neither external nor internal load, it always happens when the deflection δ is null. Therefore, the angular position of the first joint will follow the corresponding motor angle. However, if the stiffness controller commands a desired deflection, the VS units will hold the imposed preload. Since the actuators are non-backdrivable, when an external wrench acts on the end-effector, the motor output shaft is not driven by the external perturbation so the device displaces coherently with the commanded stiffness exploiting the embedded elasticity.

Given a desired pose of the wrist in minimum parametrization u_{ref} , (10) yields the desired joint angles hence the reference position of the motors $\Theta_{ref} \in \mathbb{R}^3$ as

$$\Theta_{ref} = Q_{1,ref} + \delta_{ref} \begin{bmatrix} 1 \\ 1 \\ 1 \end{bmatrix} = \mathcal{IK}_1(u_{ref}) + \Delta_{ref} . \quad (22)$$

Finally, a simple proportional control law yields the commanded motor angle

$$\Theta_{cmd} = K_P (\mathcal{IK}_1(u_{ref}) + \Delta_{ref} - \Theta) , \quad (23)$$

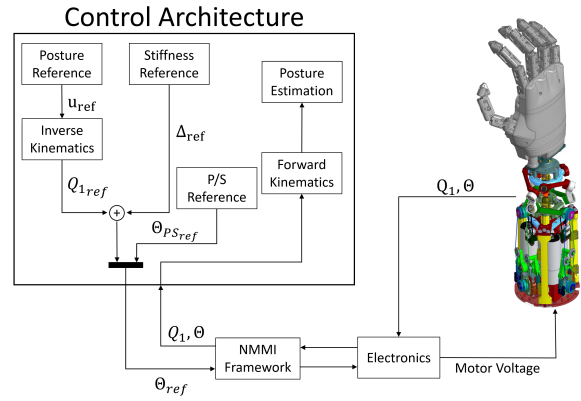


Figure 8. Scheme of the control architecture. The position and stiffness references are set in a real-time Simulink model, which communicates with the electronic hardware by using the NMMI framework. The bidirectional communication provides the encoder measurements to the user in the Simulink environment.

where K_P was tuned empirically and Θ is measured with the magnetic encoders.

Regarding the control of the PS DoF, since the motor angle coincides with the rotation angle of the hand, given the reference position $\theta_{PS,ref}$, the commanded motor angle is

$$\theta_{PS,cmd} = K_{PS}(\theta_{PS,ref} - \theta_{PS}) . \quad (24)$$

6.3 Hardware Implementation

The hardware implementation, resumed in Figure 8, was carried out in MATLAB Simulink using the NMMI framework [Della Santina et al. \(2017b\)](#), which allows for real-time bidirectional communication between Simulink and the electronic components of the VS-Wrist. The Simulink model determines the frequency of the hardware control loop, which we could increase up to 200 Hz preserving the real-time execution of all the tasks.

7 System Calibration

We calibrate the stiffness control and the posture reconstruction to account for errors due to manufacturing tolerances and other un-modeled phenomena. All calibrations use the experimental setup described in Section 8.1. The observed deviations of the system from the nominal behavior and their possible causes are reported and discussed in Section 9.

7.1 Stiffness Control Calibration

Although the system can theoretically modulate its stiffness without moving the end-effector, we observe a slight deviation of the coupler when controlling the system based on the nominal model (see Figure 9, dashed lines). Therefore, we adjust the reference posture angles as

$$\alpha_{yc} = \alpha_{yr} + P_y^4(\delta_{ref}) \quad (25)$$

$$\alpha_{zc} = \alpha_{zr} + P_z^4(\delta_{ref}) , \quad (26)$$

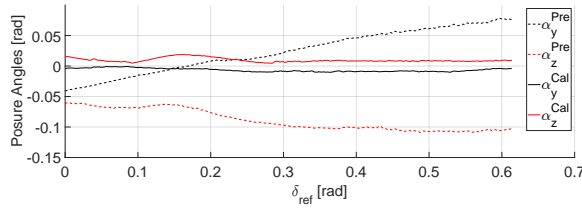


Figure 9. Calibration of the stiffness controller. The graph shows that, before the calibration, a pure stiffness command also changes the posture of the wrist due to manufacturing variability (dashed lines). Repeating the experiments after applying the compensation command proved that the proposed calibration process mitigated this undesired phenomenon (continuous lines).

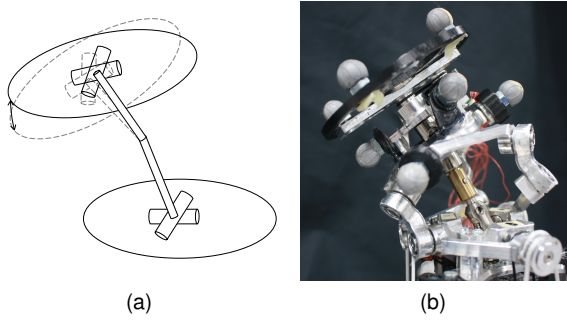


Figure 10. Panel (a) schematically represents the non-ideality manifested by the double UJ transmission, highlighting that the lower UJ angles are larger than the upper ones. Panel (b) depicts a demonstration of this phenomenon on the prototype.

where α_{yc}, α_{zc} are the compensated angles from the original references α_{yr}, α_{zr} and $P_y^4(\delta_{ref}), P_z^4(\delta_{ref})$ are 4-th order polynomials of the variable δ_{ref} which give the compensation command.

7.2 Posture Reconstruction Calibration

The posture reconstruction algorithm described in Section 3.4 relies on the nominal kinematics of the PM, which should ensure symmetry of all the angles of the three legs and, consequently, of the two UJs. However, we observe some deviation from this symmetry, which increases with the commanded stiffness. In particular, the upper UJ angles are smaller than the lower ones, as shown in Figure 10.

Therefore, we correct the posture reconstructed from the encoder readings and the nominal Forward Kinematics (FK) model, as in the following. Given the nominal UJs configuration β^I , we estimate the effective angles as

$$\hat{\beta}_i = (a_i \delta_{ref} + b_i) \beta_i^I \quad i = 1, 2, 3, 4, \quad (27)$$

where a_i and b_i minimize the least square error over the calibration trials (see Figure 11). Therefore, we compute the posture of the wrist as a function of $\hat{\beta}_i$ using (4) and (8).

8 Experimental Validation

8.1 Experimental Setup

We measure the posture of the wrist using a Vicon³ motion capture system consisting of 12 optical cameras and 14 reflective markers.

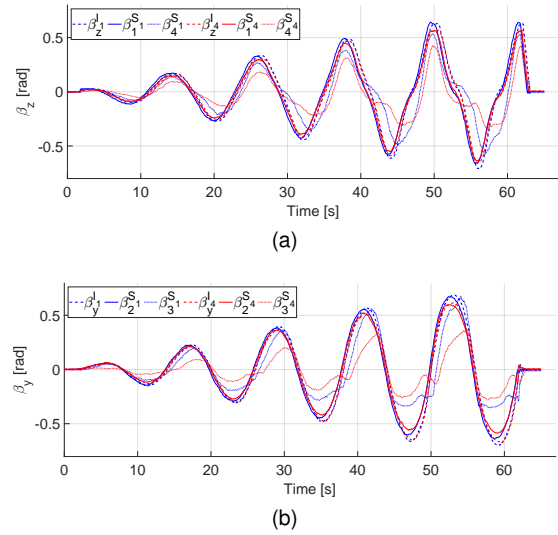


Figure 11. Comparing the effective UJ angles, measured with the motion capture system (continuous lines for the lower UJ, dot-dashed lines for the upper one), with their nominal values (dashed lines). The graphs show that the lower UJ angles are very close to the theoretical value, while the upper angles are smaller and present a perturbed pattern. This behavior is emphasized at high stiffness because of the internal tension and bending. The identified parameters from (27) are: $a_1 = -4.2 \cdot 10^{-4}$, $a_2 = -2.5 \cdot 10^{-2}$, $a_3 = -0.55$, $a_4 = -0.39$; $b_1 = 0.94$, $b_2 = 0.94$, $b_3 = 0.73$, $b_4 = 0.73$.

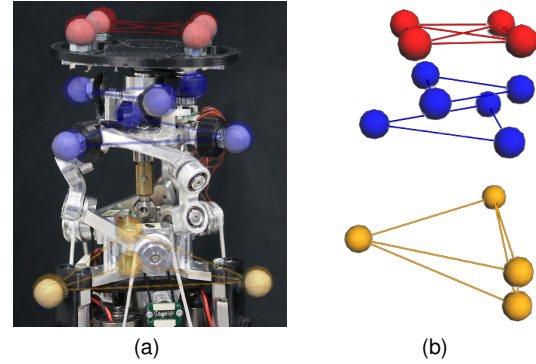


Figure 12. Panel (a) shows the employed marker set, and panel (b) displays its reconstruction carried out by the motion capture system in the Vicon Nexus environment.

Thanks to custom 3D-printed supports, three groups of markers are strapped onto the base frame, the coupler, and the end-effector, respectively (see Figure 12). The camera data are sampled at a frequency of 100 Hz and exported in Matlab for post-processing. From the marker trajectories, we reconstruct the absolute position and orientation of the reference frames $\{S_b\}$ and $\{S_e\}$ to compute the posture of the end-effector \mathbf{x} , and the transformation matrix $T_b^e(\mathbf{x})$ as in (1).

8.2 Posture Control

To evaluate the performance of the position controller, we tested the device with step functions, sine waves, and spiral posture references with various stiffness presets. Given the

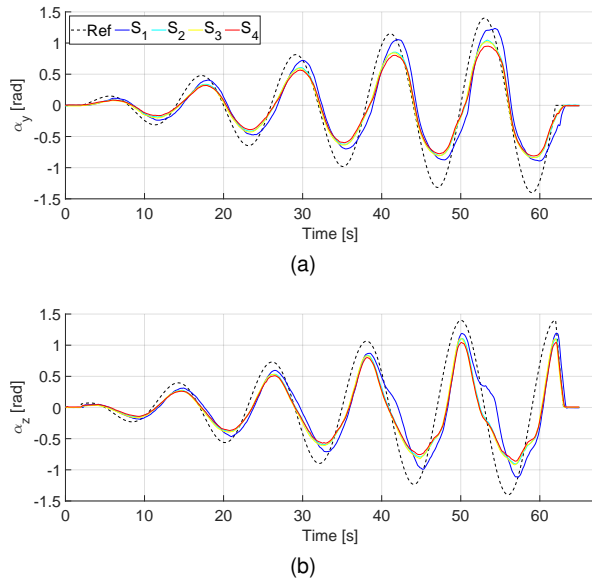


Figure 13. Tracking a helicoidal posture reference at 4 different stiffness levels (increasing from S_1 to S_4). The graphs show that, despite using the same posture reference (dashed line), the effective angles slightly decrease as the stiffness grows.

reference signals for the minimum parametrization u_{ref} and the desired springs preload δ_{ref} , (22) yields the motor reference angles.

The proportional controller provides fast and accurate motor reference tracking, with a $RMS(\theta_{error}) = 1.21^\circ$, and a rising time of $t_{rise} = 0.15$ s. Consequently, Figure 13 shows the resulting posture angles when pursuing the same reference in various stiffness configurations.

8.3 Posture Reconstruction

During the previous experiments, we also evaluated the accuracy of the posture reconstructed through the encoder measurements, considering the measurements of the motion capture system as ground truth.

Figure 14 shows the performance of the posture estimation algorithm. By exploiting the Forward Kinematics of both the PM and PS transmission, we were able to reconstruct the posture of the wrist, obtaining among trials with different stiffness configurations an average RMSE of 6.39° .

8.4 Stiffness Control

To test the stiffness modulation capability, we commanded the wrist to hold the neutral position while increasing the spring preload linearly with time. As deflection increases, the required motor torques grow until the current saturation limit is imposed by the firmware coherently with the value reported in the motor datasheet. Therefore, we identify the maximum deflection command the device could support as $\delta_{ref}^{max} = 0.6$ rad.

8.5 Variable Stiffness Ability

The VS-Wrist exploits the redundant elastic actuation to vary the stiffness of the coupler and adapt to tasks of different natures. To prove this feature, the device tracked a circular trajectory with the end-effector, at four different stiffness

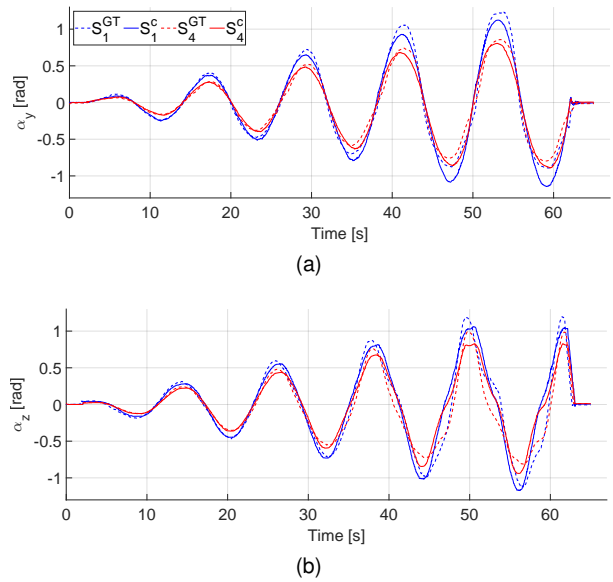


Figure 14. Reconstructing the posture of the end-effector using the measurements of the encoders (continuous lines) at different stiffness configurations (S_1 low stiffness, S_4 high stiffness). The measurements from the motion capture system are considered to be accurate thus, are set as Ground Truth (dashed lines).

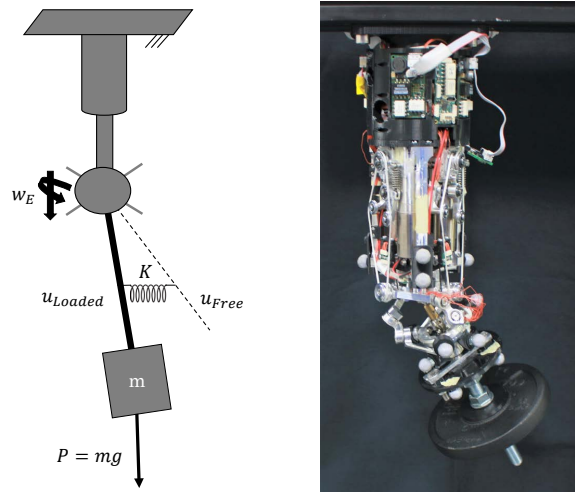


Figure 15. Experimental setup employed to quantify the Variable Stiffness ability of the device. The VS-Wrist is hung upside-down to a fixed frame while a load is attached to the coupler. Due to the external load, the coupler shifts its equilibrium configuration coherently with the commanded stiffness, exploiting the embedded elasticity.

levels, in both loaded and unloaded conditions. During these experiments, the VS-Wrist is hung upside-down on a fixed frame, as shown in Figure 15. An external load of 640 g is attached to the coupler at a distance of 78.2 mm from the origin of the local frame $\{S_e\}$. Therefore, the force of gravity applies a known external wrench which varies with the posture of the wrist. We compute a reference signal for each level of stiffness such that all the circles tracked in unloaded conditions are equal. Then, we attach the load and repeat the experiments to catch the effects of an external wrench at different stiffness presets. Since the stiffness of

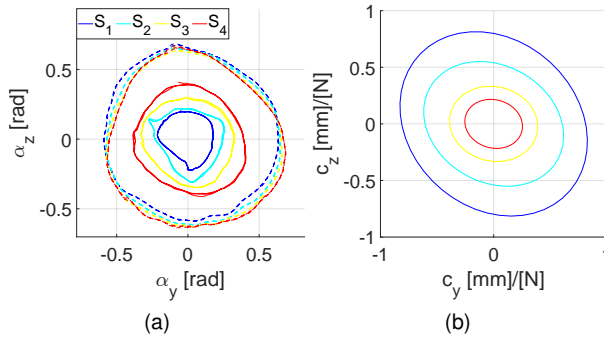


Figure 16. Panel (a) shows the posture of the coupler measured with the motion capture system during the experiments. The dashed lines represent the end-effector trajectories in the unloaded configuration at four different stiffness levels (increasing from S_1 to S_4). The continuous lines are obtained by repeating the experiments with a payload attached to the coupler. The radius of these circles is proportional to the stiffness, i.e., the capability to resist external perturbations. Panel (b) shows a graphical representation of the wrist cartesian compliance computed from the experimental data. Note that the dimension of the compliance ellipse is inversely proportional to the average stiffness of the device during the trial.

the device determines its response to external perturbations, the higher the stiffness, the smaller the difference between the trajectories in loaded and unloaded configurations. Figure 16a shows that the circles tracked at various stiffness in the unloaded condition have the same radii, but they reduce their size inversely proportional to the commanded stiffness when the load is applied. To roughly quantify the stiffness of the device, we assume that it remains constant during each trial. This hypothesis does not consider that the stiffness also depends on the posture of the coupler. However, it is useful to easily obtain an idea of the overall stiffness of the various configuration of the device. Thanks to this assumption, it holds

$$\Delta w_u = K_u \Delta u \quad (28)$$

where $\Delta w_u, \Delta u \in \mathbb{R}^{2 \times N_{sample}}$ are matrices whose columns contain the difference between the loaded and unloaded condition of, respectively, external wrench and posture, along the minimum parametrization u , for each sample of the trial, while K_u represents the stiffness of the device in minimum parametrization. Therefore, inverting (28) yields the stiffness matrix K_u that best fits the experimental data. To obtain a graphical representation in the cartesian space, we compute the cartesian compliance matrix and the compliance ellipsoids using the singular value decomposition of this matrix, as previously done Lemerle et al. (2021). Precisely, the eigenvalues determine the length of the semi-axis, while the eigenvectors define their orientation. Figure 16b shows that, coherently with the previous outcome, the various springs preload achieve different compliance of the coupler, promoting the task adaptability of the device.

8.6 Qualitative evaluation of Motion and Stiffness Behavior

To provide a more intuitive representation of the operating principle of the device and emphasize its anthropomorphism,

we developed an experimental framework of tele-impedance control, where we matched the posture of the human operator's wrist and the stiffness of his forearm into command signals for the robotic device.

To define the desired pose of the robotic wrist, we attached a custom marker set to the operator's forearm and hand. Therefore, the user's wrist angles are measured with the motion capture system to compute the reference signal for the posture of the robotic device. Furthermore, we registered the operator's myoelectric activity of the wrist flexor and extensor to measure the muscular cocontraction, which we related to the desired stiffness of the VS-Wrist, similarly to Capsi-Morales et al. (2020). To do so, we employed two commercial electrodes 13E200 from Ottobock, which are commonly used to control prosthetic limbs. We acquired the input data on a local computer in the Simulink environment, and then we sent them in real-time to the remote computer that runs the control loop via UDP stream. Figures 17 and 18 resume the outcome of this application. However, the reader can find the full video demonstration in the supplemental multimedia material.

9 Discussion

The experimental evaluation of the prototype performance confirmed that the VS-Wrist could achieve 3 DoFs in position while changing its overall stiffness with continuity.

Based on the nominal Inverse Kinematics of the PM, the proposed position controller satisfactorily matches the desired posture references. Undoubtedly, the absence of posture feedback inside the control law induces a residual error in the end-effector trajectory. On the other hand, our choice to privilege a simple implementation also preserves the intrinsic compliance of the device and requires low computational power, and thus could be suitable for the prosthetic application. Moreover, the inaccuracy in tracking a desired posture would be a minor problem for applications where a human operator closes the control loop, such as prosthetics or teleoperation.

The implemented stiffness controller allows for modulating the stiffness of the prototype continuously in a wide operational range. The preliminary calibration process compensated for the asymmetry of the VS units due to manufacturing variability and tendon stretching, canceling any undesired movements. Moreover, the experiments resumed in Figure 16, proved that the device could track a desired trajectory while holding various imposed stiffness levels. The different impact of the external load on the posture of the VS-Wrist proves the efficacy of stiffness regulation that features the task adaptability of the device. We represented the stiffness of the manipulator by employing the cartesian compliance because it can be plotted in a plane since the device has 2 DoFs, and thus, the stiffness along a principal direction is infinite. Consequently, the cartesian compliance along that direction is null, and thus it is easier to manipulate this matrix algebraically.

During the first experimentation phase, we encountered some non-idealities that we tried to explain and mitigate with a calibration phase. Figure 11 shows that the observed kinematic behavior of the PS transmission is not perfectly nominal. This phenomenon is not directly related to the

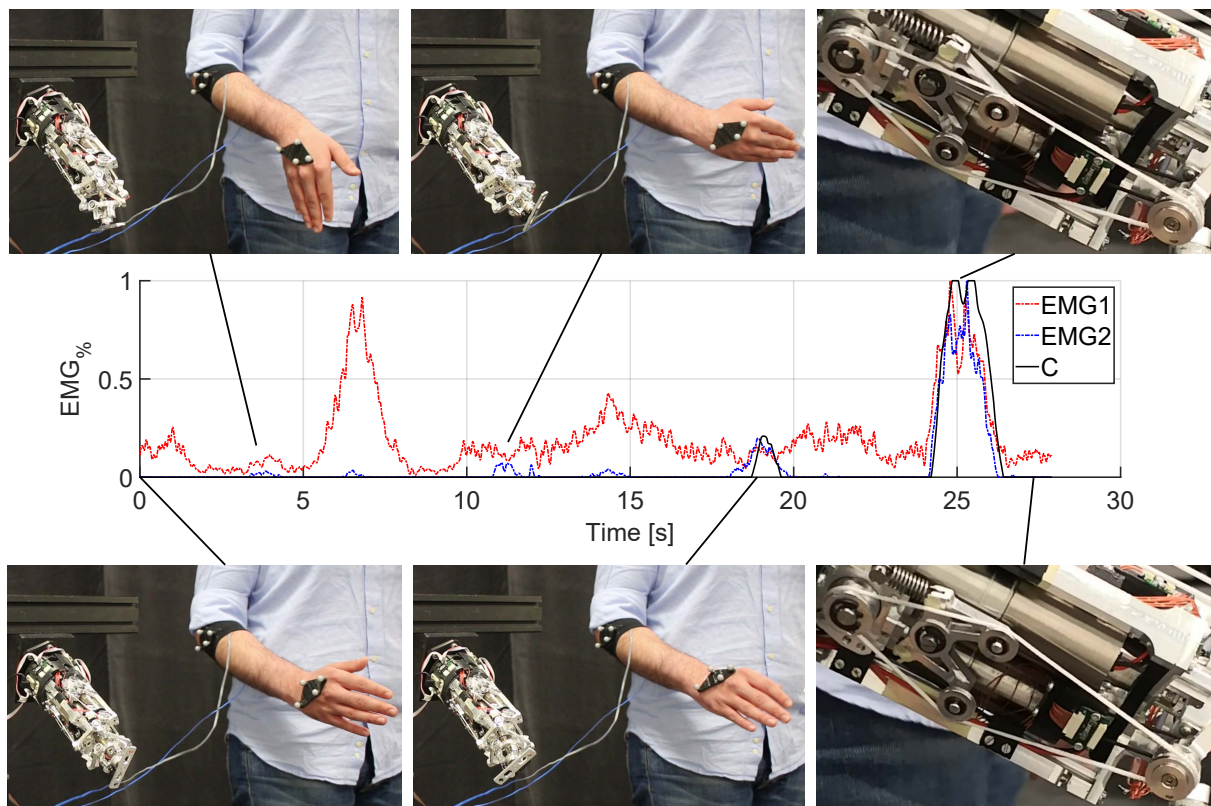


Figure 17. Photosequence of the VS-Wrist tracking the user's posture and muscular cocontraction. The graph in the middle reports the corresponding normalized EMG signals measured from a couple of antagonistic muscles of the user's forearm, highlighting the muscular cocontraction, which defines the reference stiffness configuration of the robotic wrist. Each panel depicts a specific instant of the experiment and is associated with the corresponding EMG measurement. The panels on the right describe the functioning of the elastic transmission that achieves stiffness regulation. The bottom-right frame shows the device in the soft configuration, so the tension on the tendons is low. The panel on the top-right portrays the VS-Wrist in the rigid configuration, matching the operator's muscular impedance. Coherently, the tendons of a side of all the VS units stretched to increase the stiffness.

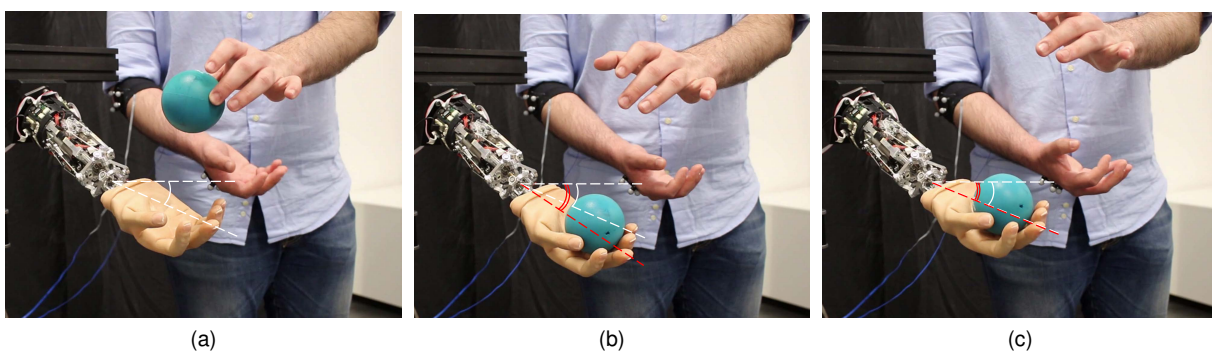


Figure 18. Proving the variable stiffness ability with a qualitative experiment. During the trial, the VS-Wrist holds a reference posture (a) at two different stiffness configurations that characterize the response of the device to an external perturbation, represented by a ball in free fall. As a consequence of the variable stiffness, the device reaches different equilibrium configurations, reported in panel (b) for the soft configuration and (c) for the rigid one.

quality of the PS transmission itself, but it is just a manifestation of the non-idealities of the real system. Nevertheless, it could be exploited to quantify these defects and improve posture estimation. Therefore, we applied a correction factor to consider the non-nominality of the device when reconstructing its posture, obtaining a faithful estimation. Finally, the proposed solution provides real-time

posture feedback bypassing the need for additional attitude sensors such as IMUs.

However, we consider some mechanical refinements for the next version of the prototype since some components bent at high stiffness while others presented some mechanical backlashes in the soft configuration. Consequently, Figure 13 shows that the posture error was proportional to the commanded stiffness because the

structural bending altered the PM kinematics. Moreover, despite the evolution of α_y traces satisfactorily the reference waveform, the device exhibits some undesired pattern along the α_z trajectories due to mechanical backlashes, which are more influential at low stiffness.

Notwithstanding the minor mechanical problems that the prototype manifested, operating the device with the tele-impedance controller emphasized that its functioning resembles humans' motion and impedance regulation principles, as shown in Figure 17. Moreover, Figure 18 gives a qualitative idea of the variable stiffness ability of the device, highlighting the differences in responding to an external perturbation. Figure 18b shows that the VS-Wrist compliantly displaces, adapting to the external environment, while in the soft configuration. On the contrary, Figure 18c demonstrates that maintaining high stiffness allows the device to resist perturbations and hold the initial posture.

10 Conclusion and Future Developments

This work addresses the problem of modeling and controlling a variable stiffness 3 DoF wrist employing redundant elastic actuation. Its controllable stiffness and inherent compliance allow the device to interact safely with the environment and to adapt to tasks of different natures. The proposed device is compact and lightweight, thus suitable for prosthetic applications. In this regard, the VS-Wrist would drastically improve the dexterity and the naturalness of upper limb prostheses since current commercial devices are mostly passive and rigid joints with reduced DoFs or, at the most, actuated along the PS axis. A similar, scaled-up design could also fit the implementation of other joints, such as the hip, shoulder, and ankle.

Future developments of this work concern the prosthetic application of the prototype, starting with mapping the user's EMG signals into control commands for the prosthesis. Furthermore, we plan to integrate this device with the VS-Elbow, described in Lemerle et al. (2019), to craft the first transhumeral variable stiffness prosthesis. Although coordinately controlling many DoFs is still an open subject, recent advantages of modern neuroscience technologies might increase the naturalness of operating more complex prostheses.

Acknowledgements

The authors would like to thank Vinicio Tincani, Mattia Poggiani, Manuel Barbarossa, Emanuele Sessa, Marina Gnocco, Giovanni Rosato, and Anna Pace for their fundamental technical support given during the hardware implementation of this work. An additional thank goes to Simon Lemerle for his work on the design concept of the device.

Declaration of conflicting interests

The authors declare that the research was conducted in the absence of any commercial or financial relationships that could be construed as a potential conflict of interest.

Funding

This research has received funding from the European Union's ERC program under the Grant Agreement No. 810346 (Natural Bionics). The content of this publication is the sole responsibility of the

authors. The European Commission or its services cannot be held responsible for any use that may be made of the information it contains.

Supplemental material

The Supplementary Material for this article, containing a video demonstration of the prototype, can be found online at: https://youtu.be/skyyDn_nia8.

Notes

1. Össur, i-Limb Quantum Flexion Wrist, <https://irp-cdn.multiscreensite.com/acf635e2/files/uploaded/Flexion%20Wrist.pdf>. Last Accessed: May 2023.
2. Mouser, AS5045, 12-Bit Programmable Magnetic Rotary Position Sensor, https://www.mouser.it/datasheet/2/588/AS5045_DS000101_2_00-1513286.pdf. Last Accessed: May 2023.
3. Vicon, Motion Capture System. <https://www.vicon.com/>. Last Accessed: May 2023

References

- Agboola-Dobson A, Wei G and Ren L (2019) Biologically Inspired Design and Development of a Variable Stiffness Powered Ankle-Foot Prosthesis. *Journal of Mechanisms and Robotics* 11(4). DOI:10.1115/1.4043603. URL <https://doi.org/10.1115/1.4043603>. 041012.
- Ajoudani A, Fang C, Tsagarakis N and Bicchi A (2018) Reduced-complexity representation of the human arm active endpoint stiffness for supervisory control of remote manipulation. *The International Journal of Robotics Research* 37(1): 155–167.
- Albu-Schaffer A, Eiberger O, Grebenstein M, Haddadin S, Ott C, Wimbock T, Wolf S and Hirzinger G (2008) Soft robotics. *IEEE Robotics & Automation Magazine* 15(3): 20–30. DOI: 10.1109/MRA.2008.927979.
- Archer SL, Dyck AD, Grant RH, Iversen EK, Jacobs JA, Kunz SR, Linder JR and Sears HH (2011) Wrist device for use with a prosthetic limb. US Patent 7,914,587.
- Baggetta M, Berselli G, Palli G and Melchiorri C (2022) Design, modeling, and control of a variable stiffness elbow joint. *The International Journal of Advanced Manufacturing Technology* DOI:10.1007/s00170-022-09886-7. URL <https://doi.org/10.1007/s00170-022-09886-7>.
- Bajaj NM, Spiers AJ and Dollar AM (2019) State of the art in artificial wrists: A review of prosthetic and robotic wrist design. *IEEE Transactions on Robotics* 35(1): 261–277. DOI: 10.1109/TRO.2018.2865890.
- Blank AA, Okamura AM and Whitcomb LL (2014) Task-dependent impedance and implications for upper-limb prosthesis control. *The International Journal of Robotics Research* 33(6): 827–846.
- Borzelli D, Cesqui B, Berger DJ, Burdet E and d'Avella A (2018) Muscle patterns underlying voluntary modulation of co-contraction. *PLoS One* 13(10): e0205911.
- Capsi-Morales P, Piazza C, Catalano MG, Bicchi A and Grioli G (2020) Exploring stiffness modulation in prosthetic hands and its perceived function in manipulation and social interaction. *Frontiers in Neurobotics* : 33.

- Chen B, Wang B, Zheng C and Zi B (2021) Design and simulation of a robotic knee exoskeleton with a variable stiffness actuator for gait rehabilitation. In: *2021 27th International Conference on Mechatronics and Machine Vision in Practice (M2VIP)*. pp. 24–29. DOI:10.1109/M2VIP49856.2021.9665028.
- Della Santina C, Bianchi M, Grioli G, Angelini F, Catalano M, Garabini M and Bicchi A (2017a) Controlling soft robots: balancing feedback and feedforward elements. *IEEE Robotics & Automation Magazine* 24(3): 75–83.
- Della Santina C, Piazza C, Gasparri GM, Bonilla M, Catalano MG, Grioli G, Garabini M and Bicchi A (2017b) The quest for natural machine motion: An open platform to fast-prototyping articulated soft robots. *IEEE Robotics & Automation Magazine* 24(1): 48–56.
- English C and Russell D (1999) Mechanics and stiffness limitations of a variable stiffness actuator for use in prosthetic limbs. *Mechanism and Machine Theory* 34(1): 7–25. DOI:[https://doi.org/10.1016/S0094-114X\(98\)00026-3](https://doi.org/10.1016/S0094-114X(98)00026-3). URL <https://www.sciencedirect.com/science/article/pii/S0094114X98000263>.
- Firth C, Dunn K, Haeusler MH and Sun Y (2022) Anthropomorphic soft robotic end-effector for use with collaborative robots in the construction industry. *Automation in Construction* 138: 104218.
- Grioli G, Wolf S, Garabini M, Catalano M, Burdet E, Caldwell D, Carloni R, Friedl W, Grebenstein M, Laffranchi M et al. (2015) Variable stiffness actuators: The user's point of view. *The International Journal of Robotics Research* 34(6): 727–743.
- Haddadin S, Albu-Schäffer A and Hirzinger G (2007) Safety evaluation of physical human-robot interaction via crash-testing. In: *Robotics: Science and systems*, volume 3. Citeseer, pp. 217–224.
- Haddadin S, Weis M, Wolf S and Albu-Schäffer A (2011) Optimal control for maximizing link velocity of robotic variable stiffness joints. *IFAC Proceedings Volumes* 44(1): 6863–6871. DOI:<https://doi.org/10.3182/20110828-6-IT-1002.01686>. URL <https://www.sciencedirect.com/science/article/pii/S1474667016447087>. 18th IFAC World Congress.
- Hogan N (1985) Impedance control: An approach to manipulation: Part ii—implementation .
- Lemerle S (2021) Soft robotics technologies to enable natural behavior in a novel generation of bionic upper limbs. *Doctoral Thesis, University of Pisa, Pisa* .
- Lemerle S, Catalano MG, Bicchi A and Grioli G (2021) A configurable architecture for two degree-of-freedom variable stiffness actuators to match the compliant behavior of human joints. *Frontiers in Robotics and AI* 8: 614145.
- Lemerle S, Grioli G, Bicchi A and Catalano MG (2019) A variable stiffness elbow joint for upper limb prosthesis. In: *2019 IEEE/RSJ International Conference on Intelligent Robots and Systems (IROS)*. pp. 7327–7334. DOI:10.1109/IROS40897.2019.8970475.
- Liu Y, Guo S, Hirata H, Ishihara H and Tamiya T (2018) Development of a powered variable-stiffness exoskeleton device for elbow rehabilitation. *Biomedical microdevices* 20(3): 1–13.
- Migliore SA, Brown EA and DeWeerth SP (2005) Biologically inspired joint stiffness control. In: *Proceedings of the 2005 IEEE international conference on robotics and automation*. IEEE, pp. 4508–4513.
- NASA (1995) Man-systems integration standards - volume i. <https://msis.jsc.nasa.gov/Volume1.htm>. Last Accessed: May 2023.
- Osu R, Kamimura N, Iwasaki H, Nakano E, Harris CM, Wada Y and Kawato M (2004) Optimal impedance control for task achievement in the presence of signal-dependent noise. *Journal of Neurophysiology* 92(2): 1199–1215.
- Rosheim ME and Sauter GF (2002) New high-angulation omnidirectional sensor mount. In: Ricklin JC and Voelz DG (eds.) *Free-Space Laser Communication and Laser Imaging II*, volume 4821. International Society for Optics and Photonics, SPIE, pp. 163–174. DOI:10.1117/12.465912. URL <https://doi.org/10.1117/12.465912>.
- Sofka J, Skormin V, Nikulin V and Nicholson D (2006) Omni-wrist iii - a new generation of pointing devices. part i. laser beam steering devices - mathematical modeling. *IEEE Transactions on Aerospace and Electronic Systems* 42(2): 718–725. DOI: 10.1109/TAES.2006.1642584.
- Tavakoli M and de Almeida AT (2014) Adaptive under-actuated anthropomorphic hand: Isr-soft-hand. In: *2014 IEEE/RSJ International Conference on Intelligent Robots and Systems*. IEEE, pp. 1629–1634.
- Tröbinger M, Jähne C, Qu Z, Elsner J, Reindl A, Getz S, Goll T, Loinger B, Loibl T, Kugler C et al. (2021) Introducing garmi-a service robotics platform to support the elderly at home: Design philosophy, system overview and first results. *IEEE Robotics and Automation Letters* 6(3): 5857–5864.
- von Drigalski F, Tanaka K, Hamaya M, Lee R, Nakashima C, Shibata Y and Ijiri Y (2020) A compact, cable-driven, activatable soft wrist with six degrees of freedom for assembly tasks. In: *2020 IEEE/RSJ International Conference on Intelligent Robots and Systems (IROS)*. pp. 8752–8757. DOI: 10.1109/IROS45743.2020.9341487.
- Yang G, Li B, Zhang Y, Pan D and Huang H (2022) A novel soft wrist joint with variable stiffness. In: Liu H, Yin Z, Liu L, Jiang L, Gu G, Wu X and Ren W (eds.) *Intelligent Robotics and Applications*. Cham: Springer International Publishing. ISBN 978-3-031-13822-5, pp. 346–356.
- Yellewa ME, Mohamed A, Ishii H and Assal SF (2022) Design and hybrid impedance control of a compliant and balanced wrist rehabilitation device. In: *IECON 2022–48th Annual Conference of the IEEE Industrial Electronics Society*. IEEE, pp. 1–6.
- Zongxing L, Wanxin L and Liping Z (2020) Research development of soft manipulator: A review. *Advances in Mechanical Engineering* 12(8): 1687814020950094.

Appendix A: Derivation of the Static Equilibrium Equations

This appendix details the derivation of the static equilibrium equations reported in Section 3.5. To start, compute the Jacobian matrix of each leg of the manipulator in the coupling point with the end-effector $J_p(q)$. These matrices depend only on the joint variables of the respective leg and relate these joint velocities to the twist of the coupling point. For the kinetostatic duality, their transpose relates the torques acting on the joints τ with the wrench w_p acting on the coupling point, such that $\tau = J_p^T(q)w_p$. Using the Denavit-Hartenberg convention, for a revolute joint, the i th column of the Jacobian matrix can be computed as

$$J_p^i = \begin{bmatrix} k_{i-1} \times (O_{i-1}P) \\ k_{i-1} \end{bmatrix}, \quad (1)$$

where k_{i-1} is the versor of z_{i-1} axes, $(O_{i-1}P)$ is the distance from the origin of frame $\{S_{i-1}\}$ of the considered point P, all expressed w.r.t. the fixed frame $\{S_b\}$. The position of the coupling point P w.r.t. the local frame $\{S_3\}$ is constant and equal to the radius of the coupler $r_e = 22.5$ mm. Therefore, the distance of the coupling point of the considered leg from the origin of the fixed frame is

$$O_0P = T_b^3(q) \begin{bmatrix} 0 \\ 0 \\ r_c \\ 1 \end{bmatrix}. \quad (2)$$

Similarly, for the local frames holds

$$O_iP = O_0P - [T_b^i(q)]_{(:,4)} \quad \text{for } i = 1, 2, 3, \quad (3)$$

where $[T_b^i(q)]_{(:,4)}$ indicates the fourth column of the transformation matrix hence the position of the origin O_i of the reference frame $\{S_i\}$, w.r.t. the reference frame $\{S_b\}$. Accounting for the equilibrium of the whole manipulator yields

$$\begin{bmatrix} \tau_A \\ \tau_B \\ \tau_C \end{bmatrix} = \begin{bmatrix} J_p^A(q_A)^T & 0_{6 \times 4} & 0_{6 \times 4} \\ 0_{6 \times 4} & J_p^B(q_B)^T & 0_{6 \times 4} \\ 0_{6 \times 4} & 0_{6 \times 4} & J_p^C(q_C)^T \end{bmatrix} \begin{bmatrix} w_A \\ w_B \\ w_C \end{bmatrix}, \quad (4)$$

where $\tau_* \in \mathbb{R}^4$ are the joint torques acting on a generic leg $*$, $w_* \in \mathbb{R}^6$ is the wrench acting on the coupling point of leg $*$, and $J^T(q) \in \mathbb{R}^{12 \times 12}$ is the full Jacobian of the parallel manipulator. Define the matrix G_* which conveys the effect of the wrench w_* acting on P_* , on the center of the end-effector O_e as

$$G_* = \begin{bmatrix} I_{3 \times 3} & 0_{3 \times 3} \\ \widehat{O_e P_*} & I_{3 \times 3} \end{bmatrix}, \quad (5)$$

where $\widehat{O_e P_*}$ is the skew-symmetric matrix that executes the cross product such that $\widehat{O_e P_*}v = O_e P_* \times v$. Therefore, given an external wrench acting on the end-effector w_{ext} , and assembling the grasp matrices for all the legs as $G = [G_A \ G_B \ G_C]$, yields to

$$w_{ext} = -Gw. \quad (6)$$

Due to the constraints given by the coupling joints, $w_* = H_*^T \tilde{w}_*$ cannot be arbitrary. The rows of H_* represent a basis for the constraint reaction of the coupling joint. For a revolute joint whose rotation axis defines the versor n , it holds

$$H_* = \begin{bmatrix} 1 & 0 & 0 & 0 & 0 & 0 \\ 0 & 1 & 0 & 0 & 0 & 0 \\ 0 & 0 & 1 & 0 & 0 & 0 \\ 0 & 0 & 0 & -n_y & n_x & 0 \\ 0 & 0 & 0 & -n_z & 0 & n_x \end{bmatrix}, \quad (7)$$

where n_x , n_y , and n_z are the cartesian component of the versor n . Similarly, the matrix which accounts for the constraints of every leg is

$$H = \begin{bmatrix} H_A & 0_{5 \times 6} & 0_{5 \times 6} \\ 0_{5 \times 6} & H_B & 0_{5 \times 6} \\ 0_{5 \times 6} & 0_{5 \times 6} & H_C \end{bmatrix}. \quad (8)$$

Therefore, the static equilibrium of the parallel manipulator holds

$$\begin{cases} \tau = J^T H^T \tilde{w} & (9a) \\ w_{ext} = -GH^T \tilde{w} & (9b) \end{cases}$$

Since the system is underactuated, it is possible to act directly only on some joints of the manipulator. Therefore, it is convenient to apply to (9a) a change of base that reorders the joint torques τ , separating the balance on the actuated torques τ_a , from the non-actuated ones $\tau_{\bar{a}}$, as

$$\begin{bmatrix} \tau_a \\ \tau_{\bar{a}} \end{bmatrix} = \begin{bmatrix} T_a \\ T_{\bar{a}} \end{bmatrix} \tau = T\tau, \quad (10)$$

where

$$T_a = \begin{bmatrix} 1 & 0 & 0 & 0 & 0 & 0 & 0 & 0 & 0 & 0 & 0 & 0 \\ 0 & 0 & 0 & 0 & 1 & 0 & 0 & 0 & 0 & 0 & 0 & 0 \\ 0 & 0 & 0 & 0 & 0 & 0 & 0 & 0 & 1 & 0 & 0 & 0 \end{bmatrix} \quad (11)$$

and $T_{\bar{a}}$ completes the orthonormal basis. Left-multiply (9a) by the change of base matrix T , to obtain the system of equations reported in (15) in the main text.

Appendix B: Derivation of the Elastic Transmission Congruence Equation

This appendix describes the employed approach to obtain the model of the elastic transmission mechanism, detailed in Section 4. The proposed method yields the function $\delta(\gamma)$ by solving a congruence equation on the tendon length L_t , known by design, and the amount of winding computed as a function of δ and γ .

Define the center of the output motor shaft O_m , of the fixed lever pulley O_t , of the first joint of the parallel manipulator O_p , and of the mobile pulley O_G . Define the winding angle as the one formed by the normal versor in the contact point of the tendon on the pulley with the fixed horizontal reference. O_m , O_p , and O_t are constant and known by design, while the position of O_G depends on γ as

$$O_m O_G(\gamma) = O_m O_t + b \begin{bmatrix} \cos(\gamma + \alpha_0) \\ \sin(\gamma + \alpha_0) \end{bmatrix}, \quad (12)$$

where $b = 18$ mm is the length of the oblique lever arm and $\alpha_0 = 70.56^\circ$ is the interior angle that it forms with the horizontal arm. Defining the radius of the motor and joint pulleys R_p and of the mobile pulley r_G , the length of the segment BC is

$$BC(\gamma) = \sqrt{|O_m O_G|_2^2 - (R_p - r_G)^2}, \quad (13)$$

the angles ψ_l and ψ_l^i are

$$\psi_l = \arccos\left(\frac{(O_m O_G)_x}{|O_m O_G|_2}\right), \quad \psi_l^i = \arcsin\left(\frac{BC}{|O_m O_G|_2}\right), \quad (14)$$

and the winding angle on the lower side of the pulley β_l is their difference $\beta_l = \psi_l^i - \psi_l$ (see Figure 1). Similarly, compute the winding angle for the upper side of the mechanism, starting from

$$O_p O_G(\gamma) = O_p O_t + b \begin{bmatrix} \cos(\gamma + \alpha_0) \\ \sin(\gamma + \alpha_0) \end{bmatrix}, \quad (15)$$

to obtain

$$DE(\gamma) = \sqrt{|O_p O_G|_2^2 - (R_p - r_G)^2} \quad (16)$$

and the angles ψ_u and ψ_u^i as

$$\psi_u = \arccos\left(\frac{(O_p O_G)_x}{|O_p O_G|_2}\right), \quad \psi_u^i = \arcsin\left(\frac{DE}{|O_p O_G|_2}\right). \quad (17)$$

Finally, compute the winding angle on the upper side of the pulley $\beta_u = \psi_u^i - \psi_u$. So, the total winding angle on the mobile lever pulley is $\beta_G = |\beta_l| + \beta_u$, on the motor pulley is $\beta_m = \pi - \theta_m - |\beta_l|$, and on the joint pulley is $\beta_p = q_1 + \frac{157.5}{180}\pi - \beta_u$. Now it is possible to write the congruence equation on the right branch of the transmission mechanism by expressing the length of the tendon as a function of the previously computed terms, obtaining

$$L_t = R_p \beta_m + BC + r_G \beta_G + DE + R_p \beta_p. \quad (18)$$

Substitute $\delta = q_1 - \theta_m$ in (18) and solve analytically to obtain the desired function $\delta(\gamma)$, and then its derivative $\frac{\partial \delta}{\partial \gamma}$.

Inverting this derivative and substituting it in

$$\tau(\gamma) = -\frac{\partial U_s}{\partial \delta} = -\frac{\partial U_s}{\partial \gamma} \frac{\partial \gamma}{\partial \delta} = -\frac{\partial U_s}{\partial \gamma} \left(\frac{\partial \delta}{\partial \gamma}\right)^{-1}, \quad (19)$$

which is (20) from the main text, yields the torque delivered by the right branch of the elastic transmission on the motor shaft. The same procedure can be applied to compute the congruence equation of the left branch of the actuation system. Given δ from the measurements of the encoders, and assuming to know L_t by design, it is possible to solve (18) numerically to obtain γ , and thus the actuated torque. Finally, accounting for the contribution of the two branches yields the torque delivered to the actuated joint. Since the motor and joint pulleys have the same radii, to achieve the static equilibrium, the torque acting on the motor shaft must be of equal magnitude but opposite in verse to the one affecting the actuated joint, leading to

$$\tau_{joint} = -\tau_{motor} = \tau_r + \tau_l, \quad (20)$$

where τ_r and τ_l are the torques delivered by the right and left branches, respectively.

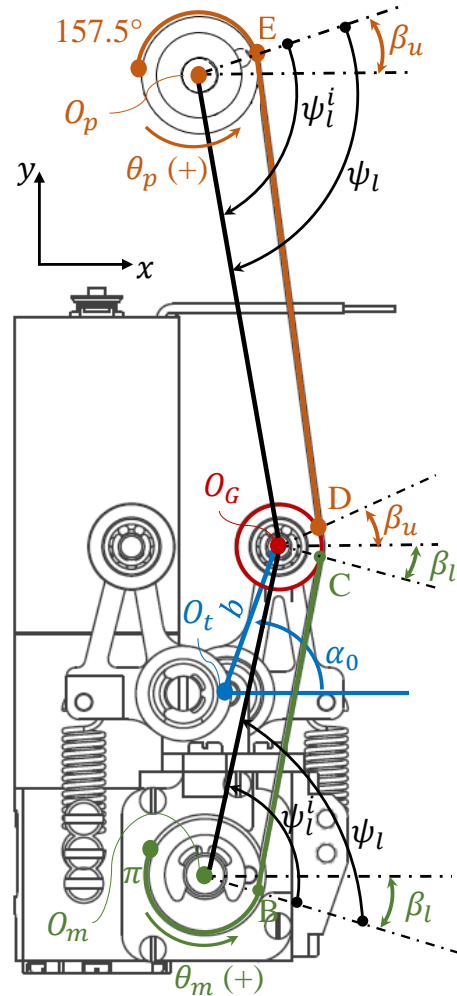


Figure 1. Schematic representation of the elastic transmission mechanism and definition of the geometric parameters needed to derive the congruence equation.